Particle simulation study of electron heating by counterstreaming ion beams ahead of supernova remnant shocks

M E Dieckmann[1], E Perez Alvaro[2], A Bret[2], G Sarri[1], I Kourakis[1] and M Borghesi[1]

1. Queen's University Belfast, Ctr Plasma Phys, Belfast BT7 1NN, UK
2 ETSI Industriales, Universidad de Castilla-La Mancha, 13071 Ciudad Real, Spain and Instituto de Investigaciones Energeticas y Aplicaciones Industriales, Campus Universitario de Ciudad Real, 13071 Ciudad Real, Spain

Abstract. The growth and saturation of Buneman-type instabilities is examined with a particle-in-cell (PIC) simulation for parameters that are representative for the foreshock region of fast supernova remnant (SNR) shocks. A dense ion beam and the electrons correspond to the upstream plasma and a fast ion beam to the shock-reflected ions. The purpose of the 2D simulation is to identify the nonlinear saturation mechanisms, the electron heating and potential secondary instabilities that arise from anisotropic electron heating and result in the growth of magnetic fields. We confirm that the instabilities between both ion beams and the electrons saturate by the formation of phase space holes by the beam-aligned modes. The slower oblique modes accelerate some electrons, but they can not heat up the electrons significantly before they are trapped by the faster beam-aligned modes. Two circular electron velocity distributions develop, which are centred around the velocity of each ion beam. They develop due to the elastic scattering of the electrons by the stationary electrostatic wave potentials. The growth of magnetic fields is observed. Their amplitude remains low because the thermal anisotropy of the electrons, which can give rise to the Weibel instability, is short-lived.

PACS numbers: 52.35.Qz, 52.50.Gj, 52.65.Rr

1. Introduction

The thermalisation of shock-reflected ion beams plays an important role in solar system and astrophysical collision-less plasma. Energetic beams, which consist of the ions that were reflected by a plasma shock, outrun the shock and interact with the upstream plasma. This upstream plasma is the interstellar medium (ISM) for supernova remnant (SNR) shocks and the solar wind for most solar system shocks. The ion beam is a source of free energy, which is released through wave instabilities. Such instabilities have been observed ahead of solar system shocks [1]. They are also important mechanisms for particle acceleration at supernova remnant (SNR) shocks [2-9].

The Buneman instability [10, 11] develops between one ion beam and one electron beam of equal density, which are both spatially uniform, unmagnetized and drift relative to each other. Such a plasma is not current neutral. A plasma with no net charge and no net current can be composed of two counter-streaming ion beams and one electron species, if the total charge density of the ions equals that of the electrons and if the partial currents of the three beams cancel out each other. This can be an appropriate description of the plasma upstream of a shock. One ion beam is composed of the shock-reflected ions and the second ion beam and the electrons are provided by the upstream plasma, into which the shock expands. Such distributions are observed ahead of the Earth's bow shock [1]. We refer with Buneman-type instability (BTI) to an electrostatic instability, which involves an ion beam with a density below that of the electrons.

A BTI develops, if the drift speed between the ion beam and the electrons exceeds the electron thermal speed. Thermal damping effects due to the ions can be neglected, as long as they are reasonably cold. If the shock-reflected ion beam is much faster than the electron thermal speed and sufficiently dense, then its current has to be cancelled out by a high drift speed between the background electrons and ions. This drift speed may exceed the electron thermal speed and result in a second BTI. The speed of SNR shocks is a few per cent of the light speed c, which exceeds by far the electron thermal speed in the ISM. We may expect that the shock-reflected ion beam and the counterstreaming ion beam are both sufficiently fast in the electron rest frame to render the plasma unstable. Such plasmas have been examined widely in the past with particle-in-cell (PIC) simulations [12]. Previous studies have addressed unmagnetized [13, 14, 15] and magnetized plasmas [16, 17] with one-dimensional PIC simulations, which can not capture the multi-dimensional nature of the wave fields. More recently, the BTI has been examined with two-dimensional PIC simulations in unmagnetized and magnetized plasma. The electrostatic simulation in Ref. [18] has modeled the interaction of one fast ion beam with cool electrons. References [19, 20] investigated ion beams that stream with nonrelativistic and mildly relativistic speeds across an orthogonal magnetic field.

We examine here with an electromagnetic 2D PIC simulation how a plasma thermalises, which consists of two counterstreaming ion beams with unequal densities that move through an unmagnetized electron plasma. The drift speeds between the electrons and each of the ion beams exceed the initial electron thermal speed by factors

of 3.4 and 17 and two BTI's develop. The faster beam has a speed that is comparable to the ones modeled with PIC simulations in Ref. [18]. The waves driven by both BTI's interact nonlinearly with the electrons, once their amplitude is adequate. Trapping by an electrostatic wave accelerates electrons along the wave vector and a thermal anisotropy in the electron's velocity distribution develops. It is the purpose of our study to assess, if a thermal anisotropy-driven Weibel instability (TAWI) [21-29] is triggered by anisotropic electron heating. Such a secondary instability can not be resolved by the electrostatic PIC code used in Ref. [18].

The initial conditions, which we consider here, are representative for a volume element in the foreshock, that is so small that the flow speed of the upstream plasma and of the shock-reflected ion beam are constant inside. However, ion beam-driven instabilities can also be triggered by the return current [30] of the cosmic rays. Similar instabilities may thus occur in a much larger volume ahead of the shock. The TAWI could provide [31] the seed magnetic field, which speeds up the cosmic ray-driven instabilities that magnetize SNR shocks [32, 33]. The inital magnetic amplitude is set to zero in our simulation, which simplifies the detection and interpretation of magnetic fields that are driven by the BTI through the subsequent TAWI.

Our results are as follows. The interaction of the background electrons with the slow and dense ion beam from the background plasma yields the faster-growing instability, as we expect from the solution of the linear dispersion relation. The electrostatic waves grow and saturate through the formation of electron phase space tubes [34-39]. The spectrum of the unstable waves is not unidirectional [18] and the phase space tubes are spatially bounded. Trapping accelerates the electrons into the direction of the propagating waves. Initially the electron velocity distribution is anisotropic and results in the growth of magnetic fields.

The electrons are scattered by the electrostatic structures, which are practically time-stationary in the reference frame of the background ions. The elastic reflections of electrons change their momentum direction but not their momentum modulus. Repeated collisions between the electrons and the phase space tubes thus redistribute the electrons into a circular interval in velocity space, which is centered at the phase speed of the waves. This mechanism differs subtly from that proposed in Ref. [18], which has attributed the crescent formation to the low phase speed of the oblique modes. The rapid electron redistribution quenches the magnetic instability and the magnetic energy saturates at a value that is orders of magnitude below the electric energy.

The plasma is no longer free of current after the redistribution. A macroscopic beam-aligned electrostatic field grows [40], which accelerates the electrons. Eventually the electrons start to interact with the faster ion beam. Electrons are accelerated primarily by trapping, but the Landau damping of the oblique modes results in a separate population of hot electrons. A crescent distribution develops, but it is much less pronounced than the one found in Ref. [18]. The likely reason is that the electron heating by the first BTI has decreased the ratio between beam speed and electron thermal speed to a value well below that used in Ref. [18]. An energetic circular

distribution in velocity space eventually develops, again due to the elastic scattering of electrons by the electrostatic structures that move with the mean velocity of the fast ion beam. No TAWI develops here, presumably because of the low velocity space density of the hot electron population. The absence of any significant magnetic field growth during the growth and saturation of the two BTIs suggests that the thermal anisotropy created by the nonlinear interaction between electrostatic waves and electrons is not capable of magnetising the foreshock of supernova remnant shocks.

The structure of the paper is as follows. Section 2 discusses the initial conditions and the PIC simulation code. Section 3 presents the simulation results. Section 4 is the discussion.

2. The initial conditions and the particle-in-cell simulation code

Our 2D3V electromagnetic PIC simulation code [41] resolves the x, y plane and the particle positions in this plane. It updates all three components of the relativistic particle momentum $\mathbf{p}$, of the electric field $\mathbf{E}$, of the magnetic field $\mathbf{B}$ and of the current $\mathbf{J}$. The code preserves $\nabla \cdot \mathbf{E} = \rho/\epsilon_0$ and $\nabla \cdot \mathbf{B} = 0$ to round-off precision and evolves the electromagnetic fields in time through

$$\nabla \times \mathbf{E} = -\frac{\partial \mathbf{B}}{\partial t}\,,\ \nabla \times \mathbf{B} = \mu_0 \epsilon_0 \frac{\partial \mathbf{E}}{\partial t} + \mu_0 \mathbf{J}. \tag{1}$$

An ensemble of computational particles (CPs) is followed in time. Each CP with the index i of the species j in the simulation has the mass and charge m_j and q_j, the momentum $\mathbf{p}_i = m_j \Gamma_i \mathbf{v}_i$ and the position $\mathbf{x}_i = (x_i, y_i)$. Each CP corresponds to a volume element of the electron phase space distribution and the ratio q_j/m_j must be equal to that of the corresponding physical particle. The position and momentum of each CP are updated according to

$$\frac{d\mathbf{x}_i}{dt} = \mathbf{v}_i\,,\ \frac{d\mathbf{p}_i}{dt} = q_j\left(\mathbf{E}[\mathbf{x}_i] + \mathbf{v}_i \times \mathbf{B}[\mathbf{x}_i]\right). \tag{2}$$

We consider here three spatially uniform plasma species with Maxwellian velocity distributions. The electrons have the density n_0 and the temperature 10 eV or the thermal speed $v_{te} = 1.325 \times 10^6$ m/s. They move at the speed $v_e = 4.5 \times 10^6$ m/s along increasing values of x, which gives $v_e = 3.4 v_{te}$. We consider a mass ratio between the ions and electrons of $m_i/m_e = 10^3$. The bulk ions are at rest in the simulation box. Their density and temperature are $n_i = 5n_0/6$ and 5.5 eV. The bulk ions would correspond to the relatively cool upstream plasma ahead of a SNR shock. The ion beam has the density $n_b = n_0/6$ and temperature 10 keV. Its mean speed is $v_b = 6v_e$. The ion beam is much hotter than the bulk ions. Plasma shocks are neither perfectly planar nor elastic reflectors, so the momentum change by the reflection differs for each ion [7], which causes a rise of the temperature. The plasma is charge neutral by $n_b + n_i = n_0$ and it is initially free of current by $n_0 v_e = n_b v_b$. In what follows, the velocities $\mathbf{v}$ and positions $\mathbf{x}$ are normalized to v_e and to the electron skin depth $\lambda_e = c/\omega_p$. The plasma frequency of the electrons with the mass m_e and charge $-e$ is ω_p. The time is multiplied

with ω_p. Frequencies are given in units of ω_p and the wave numbers are given as kc/ω_p. The electric and magnetic fields are expressed as $e\mathbf{E}/\omega_p c m_e$ and $e\mathbf{B}/\omega_p m_e$.

Both BTI's result in electrostatic waves that are practically stationary in the rest frame of the respective ion beam. The real parts of the wave frequencies ω_{u1}, ω_{u2} and the corresponding wave lengths k_{u1}, k_{u2} can be estimated in the cold plasma approximation. The bulk ions and the electrons drive waves with the frequency $\omega_{u1} \ll 1$ and the wave number $k_{u1} \approx c/v_e$ or $k_{u1} \approx 67$. The instability between the fast ion beam and the electron beam drives waves with $k_{u2} \approx c/(v_b - v_e)$ or $k_{u2} \approx 13$. Their Doppler shifted frequency is $\omega_{u2} \approx k_{u2} v_b$ or $\omega_{u2} \approx 1.2$ in the box frame of reference. The growth rate of a BTI is $\omega_i \approx \left(3\sqrt{3}\omega_b^2 \omega_p/16\right)^{1/3}$ [13], where ω_b is the plasma frequency of the ion beam. In the cold plasma limit, this growth rate is practically independent of the wavenumber orthogonal to the beam velocity vector. We can estimate with this equation the growth ratio between both BTI's as $\omega_{i1}/\omega_{i2} = (n_i/n_b)^{1/3} \approx 1.8$. The exponential growth rate of the BTI driven by the bulk ions is 1.8 times that of the ion beam-driven BTI.

The simulation box has the size $L_x \times L_y = 3 \times 4$, which is resolved by a grid with $N_x \times N_y = 580 \times 760$ quadratic cells with the sidelength $\Delta_x \approx 1.2\lambda_D$, where $\lambda_D = \lambda_e/226$ is the electron Debye length. The boundary conditions are periodic, which limits the wavenumber spectrum to $k_x = 2\pi a/3$ and $k_y = 2\pi b/4$ with the integers $1 \leq a \leq N_x/2$ and $1 \leq b \leq N_y/2$. The short unstable wave has $k_{u1} L_x \approx 200$ and about 32 wave lengths are resolved. The long unstable wave has $k_{u2} L_x \approx 39$ and about 6 wave periods are resolved. Each of the plasma species is represented by 320 CPs per cell. The simulation time step is $\Delta_t = 2.5 \times 10^{-3}$ and the simulation runs for $T_M = 1200$.

3. Numerical simulation

Electrostatic waves are polarized parallel to their wave vector and the wavenumber spectrum contains oblique modes. We thus expect the growth of electric field patches in the simulation plane, which correspond to clouds with a net charge density. These charge clouds must be enwrapped by in-plane electrostatic fields and E_y should grow to an amplitude that is comparable to that of E_x. The balance between the energy densities of both electric field components depends on the shape and orientation of the clouds. We compute the electric field energies $D_{ex}(t) = (2\epsilon_0)^{-1} \int E_x^2(x,y,t) dx\, dy$ and $D_{ey}(t) = (2\epsilon_0)^{-1} \int E_y^2(x,y,t) dx\, dy$. The energy $D_{bz}(t) = (2\mu_0)^{-1} \int B_z^2(x,y,t) dx\, dy$ of the magnetic field component orthogonal to the simulation box will reveal if the electron's thermal anisotropy results in the growth of a magnetic field. The kinetic energies of the electrons and of the bulk ions are $K_e(t) = m_E c^2 \sum_j (\Gamma_j - 1)$ and $K_i(t) = m_I c^2 \sum_j (\Gamma_j - 1)$, where m_E and m_I are the non-relativistic masses of the computational electrons and ions and Γ_j the Lorentz factor of the j^{th} CP. The sum is over all CPs of that species. All energies are computed in the rest frame of the bulk ions and they are normalized by $K_e(0) = E_{K0}$. The mean electric field in the simulation box is $\langle E_x \rangle = (N_x N_y)^{-1} \sum_{i=1}^{Ny} \sum_{j=1}^{Nx} E_x(i,j,t)$, where $E_x(i,j,t)$ is the electric field at the grid cell with the indices i and j at the time t. A low pass filter removes the oscillations

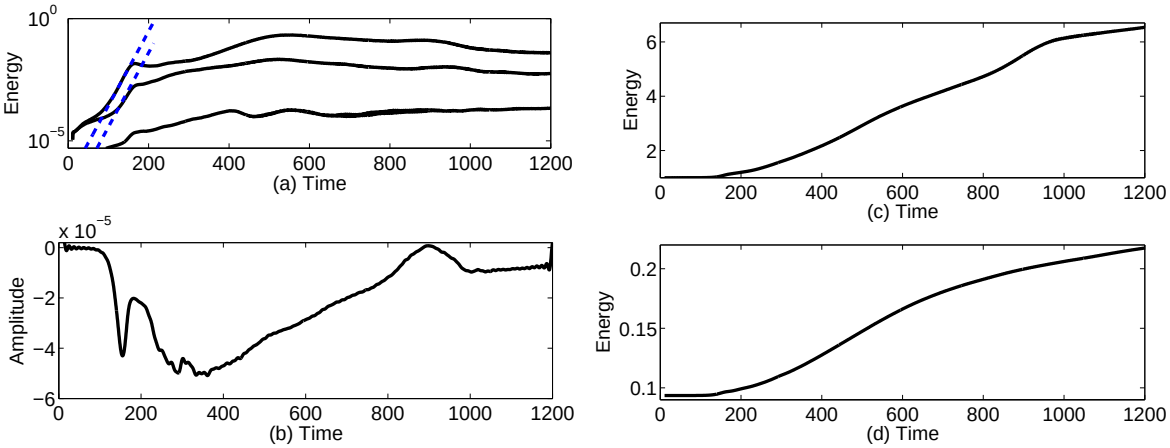

Figure 1. (Colour online) The electric D_{ex} (upper curve), D_{ey} and the magnetic D_{bz} (lower curve) energies are displayed in panel (a). The dashed blue lines are exponential fits with the same growth rate. Panel (b) shows the box-averaged electric field amplitude $\langle E_x \rangle$. The electron energy $K_e(t)$ is shown in panel (c) and that of the bulk ions in panel (d). All energies are normalized to E_{K0}.

with a frequency exceeding $\omega_f = 0.8\omega_p$, which reveals the trend of the curve.

Figure 1 shows their time evolution. A rapid exponential growth of the electric field energy is observed in the time interval $50 < t < 150$ with $D_{ex} \approx 10 D_{ey}$. Fitting $\exp(2\omega_i t)$ to the energy densities D_{ex} and D_{ey} gives us the amplitude's growth rate $\omega_i \approx 0.035$. This growth rate is well below the peak growth rate $\omega_{i1} \approx 0.064$ for cold bulk ions and electrons. Thermal effects reduce the growth rate and D_{ex} and D_{ey} are integrated over the entire simulation box, which averages the field energies over all unstable modes and not just over the fastest-growing ones. The saturation of D_{ex} and D_{ey} coincides with the growth of K_e and K_i, which evidences the saturation of the BTI driven by these two species. Figure 1(b) reveals that $d_t \langle E_x \rangle < 0$ during $100 < t < 150$, which implies by Ampére's law a net current $j_x > 0$. A rapid switch to $d_t \langle E_x \rangle > 0$ takes place at $t \approx 150$. All displayed field components and the electron energy continue to grow after $t \approx 150$. D_{ex} and D_{ey} grow by another order of magnitude until $t \approx 500$ when they reach their maximum. Their growth rates are well below that of the initial growth phase prior to $t \approx 150$ and D_{ex} is not proportional to D_{ey}. An exponential growth of D_{bz} between $200 < t < 400$ is observed and it remains approximately constant after this time. The magnetic energy remains 2-3 orders of magnitude below that of the electric field components, which implies an essentially electrostatic plasma dynamics. The electron energy K_e, which takes into account their bulk flow, grows practically linearly up to a value $6E_{K0}$ in the interval between $150 < t < 1000$.

3.1. Saturation of the instability between electrons and bulk ions

Figure 2 shows the electric fields in a part of the simulation box at $t = 150$. The structures in E_x and E_y belong to waves with wave vectors that are in some cases tilted

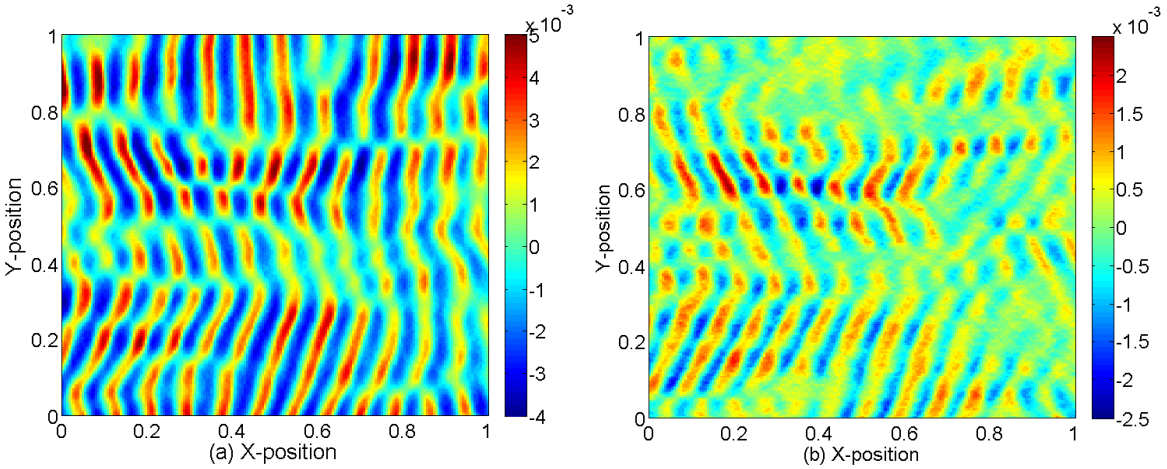

Figure 2. (Color online) The electric field distributions in a subinterval of the simulation box at $t = 150$: E_x is shown in panel (a) and E_y in panel (b).

with respect to the beam velocity vector. Their amplitude is two orders of magnitude larger than the mean electric field $\langle E_x \rangle$ in Fig. 1(b). Such wave fields have also been observed previously in electrostatic PIC simulations [18]. The E_x and E_y are projections of the obliquely oriented electric field onto the x and y axes, explaining why $D_{ex} \propto D_{ey}$ until $t = 150$. The wavelength of the structures is $\lambda \approx 0.06$ or $k \approx 100$. This value is larger than the $k_{u1} \approx 70$ expected for the waves driven by a BTI between the bulk ions and the electrons in the cold plasma limit and this shift is a thermal effect.

Various projections of the resolved electron phase space distribution $f(x, y, v_x, v_y, v_z)$ at $t = 150$ are shown in Fig. 3. The phase space projection on the x, v_x plane integrates this distribution over all v_y, v_z and over ten grid cells along y. Figures 3(a) and (b) integrate the distribution over $0 < y < 0.05$ and over $1.55 < y < 1.6$, respectively. Figures 3(a) and (b) reveal electron phase space holes, which arise when electrostatic waves saturate [34]. The width of each phase space hole corresponds to one wave period of the electrostatic waves driven by the BTI. The exponential growth phase of D_{ex} and D_{ey} ends at $t = 150$ as usual due to the trapping of electrons. The electrons are trapped by a potential, which is practically stationary in the rest frame of the bulk ions. This is evidenced by the supplementary movie 1, which shows a time animation of Fig. 3(a). The electrons gyrate around $v_x = 0$ at early times. The mean speed of the trapped electrons inside of a phase space hole is less than v_e, which can be seen in Fig. 3. A significant fraction of the electrons has been slowed down at $t = 150$, which reduces the modulus of the electron current. The electron current is negative because $v_e > 0$. The ions hardly react to the electric field because $m_i \gg m_e$ and they can not compensate the change of the electron current. We obtain a macroscopic box-averaged $\langle j_x \rangle > 0$, which explains why $d_t \langle E_x \rangle < 0$ in Fig. 1(b). The mean electric field $\langle E_x \rangle < 0$ in Fig. 1(b) accelerates all electrons in the positive direction, which will reduce $\langle j_x \rangle$. The maximum of the phase space density in Fig. 3(c) is thus found at $v_x > 1$. The electrons in this core population have not been trapped as we can see from Figs 3(a,b) and from movie

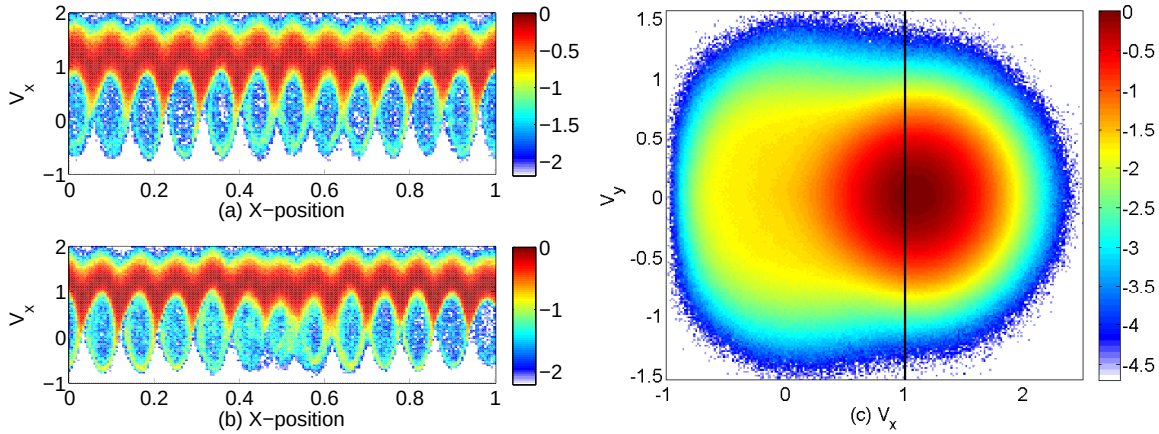

Figure 3. (Color online) Electron phase space distributions at $t = 150$: Panel (a) and (b) show phase space projections onto the x, v_x plane. The distribution is integrated over $0 < y < 0.05$ in (a) and over $1.55 < y < 1.6$ in (b). The electron distribution has been integrated over all x, y, v_z for the projection onto the v_x, v_y plane in panel (c). The vertical line corresponds to $v_x = v_e$. All distributions are normalized to their respective maxima and the colour scale is 10-logarithmic.

1, but they have all gained speed along x. The trapped electrons in Fig. 3(c) are found at $v_x < 1$. The electron distribution is stretched out along v_y, because the electrons are trapped by oblique waves (See Fig. 2).

The electrons oscillate in the wave potential with the normalized trapping frequency $\omega_T = (k_0 E_0)^{1/2}$ [42], where E_0 is the electric field amplitude of a sine wave with the wave number k_0. Figure 2 gives us $E_0 \approx 4 \times 10^{-3}$ and $k_0 \approx 100$. The electrons gyrate in the electrostatic potential with the frequency $\omega_T \approx 0.6$ and the gyration time sets the time-scale during which the phase space holes and their associated current can change. Movie 1 shows that indeed the electron phase space holes rapidly expand along v_x and increase their density during at $t \approx 150$. The bulk of the electrons is accelerated to positive speeds. A rapid change in $\langle j_x \rangle$ can be expected due to an overshoot of the current of the accelerating electrons beyond the initial electron current, which may be responsible for the change of sign of $d_t \langle E \rangle$ in Fig. 1(b) at this time.

The electrons are accelerated by $\langle E_x \rangle < 0$ (Fig. 1(b)) into the positive x-direction and they are heated by their interaction with the localized electric field structures (Fig. 2). Figure 4 demonstrates this by a comparison of the electron velocity distributions at the times $t = 200$ and $t = 300$, when the modulus of $\langle E_x \rangle$ is largest. The velocity that corresponds to the maximum of the electron phase space density is found at $v_x \approx 1.2$ at $t = 200$ and at $v_x \approx 1.6$ at $t = 300$. The electron distribution widens in velocity space and it adopts an increasingly circular shape. The centre of the hot circular distribution is at $v_x \approx 0.3$ at $t = 300$. We can not observe a density distribution in Fig. 4 that resembles the crescent found in Ref. [18].

The electron distribution in Fig. 3(c) can be subdivided into a thermal core population centred at $v_x \approx 1.2$ and $v_y \approx 0$ with a high density and a thermally

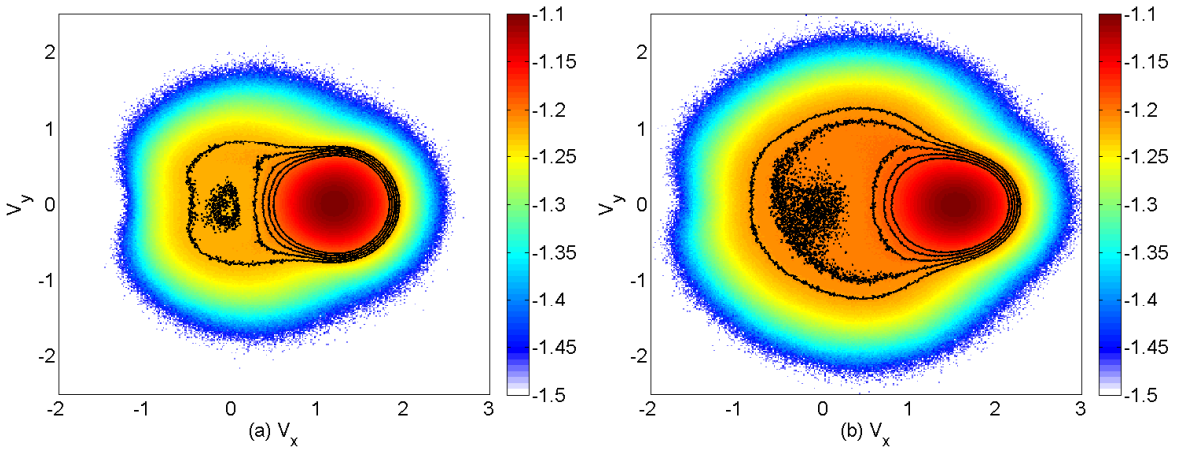

Figure 4. (Color online) Evolution of the electron velocity distribution: Panel (a) shows the electron distribution at $t = 200$ and panel (b) shows it at $t = 300$. Both distributions are normalized to the peak value at $t = 150$ and the colour scale is 10-logarithmic. The black curves are the contour lines -1.24, -1.23, -1.22, -1.21, -1.20.

anisotropic hot electron population with a lower density. The low-density electron population is elongated along v_x in Fig. 4(a) and it has become almost circular at $t = 300$ in Fig. 4(b). It is thus fair to assume that this thermally anisotropic electron population is responsible for the growth of D_{bz} in Fig. 1(a) and that the magnetic field growth ceases once the electron distribution is isotropic in velocity space. A thermally anisotropic electron distribution drives waves with a wave vector, which is aligned with the direction along which the electrons are cool [21]. We thus expect a wave vector of the magnetowaves that is almost parallel to the y-direction. The magnetic instability is driven by currents in the x-y plane and the unstable magnetic field component is thus aligned with the z-direction. Indeed only D_{bz} grows in our simulation, while the other magnetic field components remain at noise levels (not shown).

Figure 5 compares the spatial distribution of B_z at the time $t = 150$, which is just before the exponential growth phase of D_{bz} in Fig. 1(a), and at $t = 400$, when the exponential growth phase of D_{bz} ends. The magnetic field is initially weak and the structures are small. A large coherent magnetic field structure has emerged at $t = 400$. The size of this patch is of the order of an electron skin depth in both spatial directions and the magnetic amplitude gives a ratio between the electron cyclotron frequency and the plasma frequency of 6×10^{-4}, which is comparable to the ratio found in the interstellar medium [32]. The field patch is not thermal noise. Thermal noise [43] is linked to charge and current density fluctuations due to the finite number of computational particles and its coherence length is comparable to the grid cell size. The structure centred at $x = 0.7$ and $y = 1.7$ in 5(b) is, however, not the plane wave with a wave vector parallel to the y-axis, which we would expect from a TAWI [24]. Possible reasons are the weak thermal anisotropy, which we observe in Fig. 3(b), the rapid change of the electron velocity distribution due to the scattering by the electrostatic potentials and, finally, the phase space density contours that are not orthogonal to x

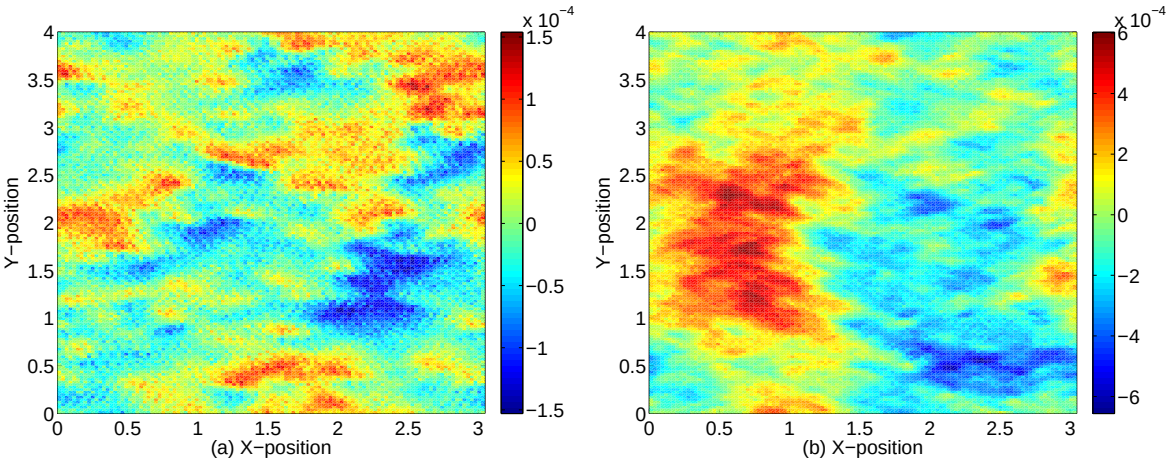

Figure 5. (Color online) The B_z component of the magnetic field at the times $t = 150$ (a) and $t = 400$ (b). The full simulation grid is displayed.

or y. A magnetic structure is growing, but we can not attribute it to an elementary instability such as a TAWI.

3.2. Saturation of the instability between electrons and beam ions

Figure 4(b) demonstrates that the mean electric field $\langle E_x \rangle$ in Fig. 1(b) has accelerated the bulk of the electrons to $v_x \approx 1.7$ and that the hot electron tail reaches $v_x \approx 3$. This speed is well below the mean speed $v_b = 6$ of the fast ion beam and a second BTI between electrons and beam ions will develop. The relative speed $\Delta v_x \approx 3$ between the electrons and ions is significantly larger than for the initial instability between the electrons and the bulk ions, but it is well below that in Ref. [18]. This second instability is responsible for the continued growth of D_{ex} after $t \approx 150$ in Fig. 1(a). However, the acceleration of the electrons by $\langle E_x \rangle$ has narrowed the velocity gap between the fastest electrons and the beam ions, which should result in a wave number of the unstable electrostatic waves, which is higher than the $k_{u2} = 1/(v_b - v_e) \approx 13$, which we estimated from a cold plasma model in section 2.

Figures 6(a,b) reveal that this second BTI has already commenced to grow at $t = 400$. Movie 1 shows a wave perturbation after $t \approx 300$ of the electron distribution that propagates at a high speed to increasing x, which corresponds to the wave driven by the BTI between the electrons and the fast beam. Strong modulations of the electron distribution with $1.5 < v_x < 3$ are present. Their wave number is $k_o = 14\pi/3 \approx 14.6$, which is indeed larger than k_{u2}. However, k_o may not correspond to the true fastest growing wave because the periodic boundary conditions enforce a discrete wave spectrum. The electron velocity distribution in Fig. 6(c) reveals that the dilute electron component forms an almost circular distribution centred at $v_x \approx 0.5$ and $y \approx 0$. The thermal anisotropy has been further reduced, which may explain why D_{bz} ceases to grow at $t = 400$ in Fig. 1(a). The contour line corresponding to $10^{-1.18}$ at

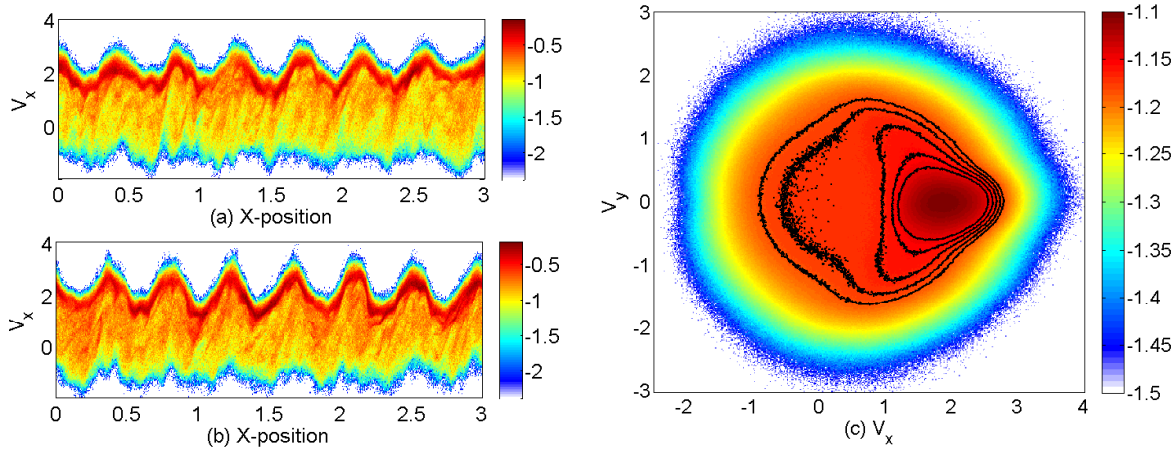

Figure 6. (Color online) Electron phase space distributions at $t = 400$: Panel (a) and (b) show phase space projections onto the x, v_x plane. The distribution is integrated over $0 < y < 0.05$ in (a) and over $1.55 < y < 1.6$ in (b). The electron distribution has been integrated over all x, y, v_z for the projection onto the v_x, v_y plane in panel (c). All distributions are normalized to their respective maxima at $t = 150$ and the colour scale is 10-logarithmic. The black curves in (c) are the contour lines -1.2, -1.19, -1.18, -1.17, -1.16.

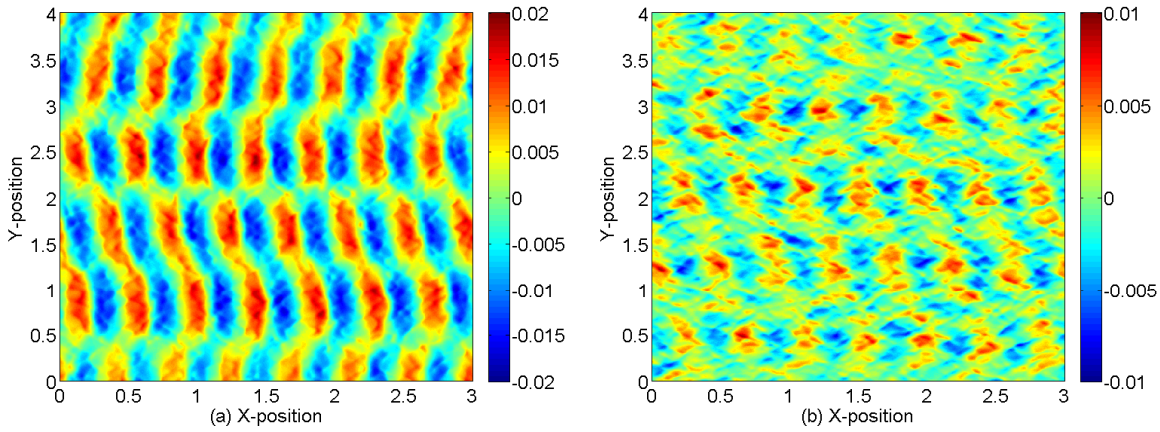

Figure 7. (Color online) The electric field distributions at $t = 500$: E_x is shown in panel (a) and E_y in panel (b).

$v_x \approx 1$ is almost aligned with the v_y-axis. It resembles the crescent in Ref. [18], but it is much less pronounced.

Figure 7 shows the electric field distribution at $t = 500$, when D_{ex} and D_{ey} reach their peak values in Fig. 1(a). The structures in E_x and E_y show a spatial correlation due to the obliquity of the wave front. The characteristic tilt angle between the wave vector and the x-axis is less than the one in Fig. 2 and thus $|E_y| \ll |E_x|$. Internal filamentary structures are visible in the intervals with $|E_x| \gg 0$. The filamentary structures are relatively stronger in E_y compared to E_x, which may explain why D_{ex} does no longer grow in unison with D_{ey} in Fig. 1(a) at this time. The electric field amplitude in Fig.

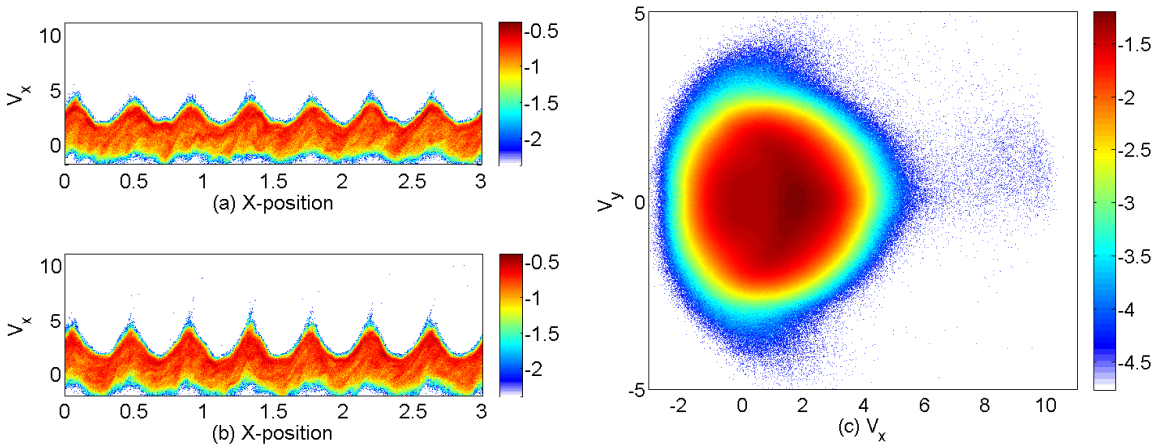

Figure 8. (Color online) Electron phase space distributions at $t = 500$: Panel (a) and (b) show phase space projections onto the x, v_x plane. The distribution is integrated over $0 < y < 0.05$ in (a) and over $1.55 < y < 1.6$ in (b). The electron distribution has been integrated over all x, y, v_z for the projection onto the v_x, v_y plane in panel (c). All distributions are normalized to their respective maxima at $t = 150$ and the colour scale is 10-logarithmic.

7(a) exceeds that in Fig. 2(a) by a factor of 4 and the wave length is larger by a factor 5. The electrostatic potential, which is driven by the BTI between the electrons and the beam ions, thus exceeds that of the faster growing BTI by a factor of ≈ 20. The trapped electron islands driven by this more powerful instability will thus be much larger than those in Fig. 3.

Some electrons are already trapped at the time $t = 500$ by this faster wave, which is the time when D_{ex} saturates in Fig. 1(a). The supplementary movie 2, which shows the spatially integrated phase space distribution as a function of v_x, v_y and corresponds to Fig. 8(c), demonstrates that the number of electrons trapped by the fast wave rapidly increases after this time. The black lines correspond to the speeds of both ion beams. Figures 8(a,b) demonstrate that the electron velocity distribution is not sinusoidal, which is a sign of a nonlinear wave, and that some electrons already have speeds of $v_x > 5$. These electrons are found close to the cusps of the electron distribution with $v_x \approx 5$, which corresponds to the unstable equilibrium point of a periodic electrostatic potential that moves with a speed $\approx v_b$. The fastest electrons have just started their periodic motion in the electrostatic potential of the wave fronts with a wave vector, which is parallel to the x-axis. The electron velocity distribution in Fig. 8(c) has been integrated over the entire simulation box and it reveals that a small fraction of electrons have been accelerated up to $v_x \approx 10$. These electrons have reached the stable equilibrium point of the electrostatic potential and their kinetic energy reaches its peak value. The electron velocity distribution also reveals the presence of non-thermal electrons at $v_x \approx 1$ and at $|v_y| \approx 4$. These electrons must have gained speed by their interaction with the oblique modes. It has been pointed out recently [18] that the oblique modes can interact more easily with electrons than the beam aligned mode, because their phase

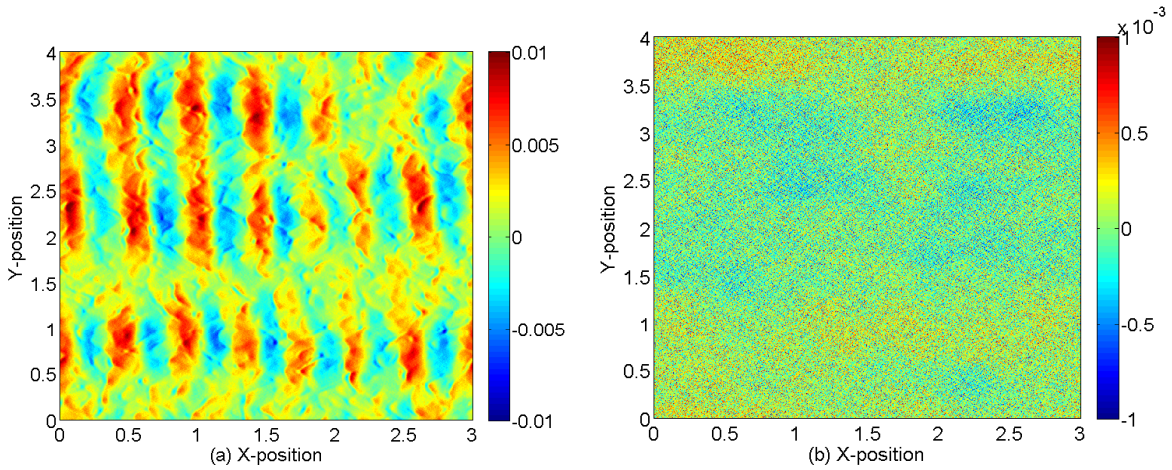

Figure 9. (Color online) The electric field distributions at $t = 1200$: E_x is shown in panel (a) and B_z in panel (b).

speed is lower. The interaction of electrons with the oblique modes results in a velocity distribution, which resembles a crescent. This saturation mechanism is dominant, if the thermal spread of the electrons is small compared to the beam speed. The beam speed was 10 times the electron thermal speed in Ref. [18]. If the electron thermal spread is comparable to the beam speed, like for the instability between the bulk ions and the electrons, then the beam aligned modes can easily trap the electrons in the high-energy tail of the electron distribution and no crescent develops. The larger gap between the speed $v_x \approx 3.5$ of the fastest electrons in Fig. 6(c)) and the ion beam speed $v_b = 6$ apparently puts the electron interaction with oblique modes and with beam-aligned modes on an equal footing. This can be seen also in movie 2, where it becomes evident that electrons are accelerated along v_x at large v_x and along v_y for $v_x \approx 0$ after $t \approx 450$.

The interaction of the electrons with the electrostatic potentials of the long waves scatters them. Scattering the electrons results in dissipation, which affects the current and charge density distribution of the plasma. Figure 9 shows the distributions of E_x and B_z at $T_M = 1200$. Strong electrostatic waves are still present. The magnetic field reveals strong noise fluctuations on a Debye-length scale, which we attribute to thermal noise. The typical amplitudes of B_z are large; the fluctuation amplitude increases with the electron temperature. We conclude from Fig. 9(b) that the TAWI, even if it has been responsible for the magnetic field growth in Fig. 5, is not an efficient source of coherent magnetic fields for the selected parameters.

The reason for the discrepancy between the lifetimes of the electrostatic and magnetic structures becomes evident from the plasma distribution functions shown in Fig. 10. The electron velocity distribution in Fig. 10(a) has its peak density at $v_x \approx 0$ and $v_y \approx 0$. The electrons accumulate at speeds, which correspond to the phase speed of the waves driven by the BTI between bulk ions and electrons. An approximately circular electron velocity distribution extends up to $\sqrt{v_x^2 + v_y^2} \approx 3$. The electron scattering is isotropic in the rest frame of the slow waves. A second circular structure, albeit with a

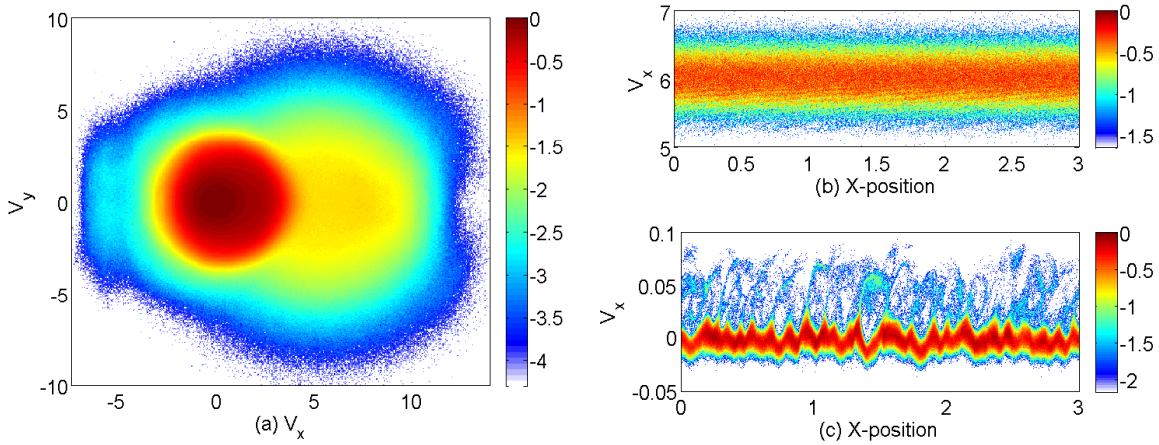

Figure 10. (Color online) Particle distribution functions at $t = 1200$: Panel (a) shows the electron velocity distribution. Panel (b) and (c) show the ion distributions integrated over the interval $0 < y < 0.05$. All distributions are normalized to their peak value at $t = 1200$ and the colour scale is 10-logarithmic.

lower number density, is observed at $v_x \approx 6$. These electrons accumulate at the phase velocity of the waves driven by the BTI between electrons and beam ions. The electron scattering is apparently isotropic in the rest frame of the fast waves. The electrons are thus scattered by two systems of electrostatic waves that have a different wave length and that move at different speeds.

The scattering should result in the rapid thermalisation of the electrons and in a dissipation of large-scale electron currents in the simulation plane. This dissipation explains why the B_z field in Fig. 9(b) is no longer coherent over large spatial scales. The electrostatic fields can also be supported by modulations of the ion velocity and density and they are thus robust against the electron scattering. The beam ions in Fig. 10(b) do not show any non-thermal features and the density modulation is in the linear regime. Their high temperature implies that the beam ions can support large electrostatic fields without developing nonlinear oscillations with velocity oscillations that exceed by far their thermal speed. The electrostatic fields connected with the density oscillations of the beam ions are the ones visible in Fig. 9(a). The bulk ions in Fig. 10(b) show strong velocity oscillations. Their low thermal pressure implies that they can not sustain large electrostatic fields without showing non-thermal signatures, like accelerated ions.

4. Discussion

We have examined the growth and saturation of electrostatic Buneman-type instabilities (BTI's) with the help of a particle-in-cell simulation. Our system of two counter-streaming ion beams is representative for the foreshock region of supernova remnant shocks. The bulk ions and the electrons are the upstream plasma, while the ion beam corresponds to the shock-reflected ions. The system has initially been charge and

current neutral and the plasma has been field-free, which is idealized. Only magnetized shocks can produce shock-reflected ion beams that move faster than the electrons in the upstream frame of reference. Electrostatic shocks have been observed experimentally and numerically [44, 45], but their speed is typically well below the electron thermal speed. The magnetic field, although realistic for the foreshock region of fast plasma shocks, has been omitted to simplify the detection of magnetic instabilities.

The simulation has shown that two wave modes are growing. One instability branch corresponds to the BTI between the bulk ions and the electrons. It is the faster growing one. The second branch develops between the fast ion beam and the electrons. The large phase speed of its waves can accelerate electrons to larger speeds and this instability is thus more powerful. Both wave branches support a continuos wave spectrum ranging from the beam-aligned modes with a high phase speed to the slower oblique modes [18]. The low relative speed between the electrons and the bulk ions implied that the instability saturated by the conventional trapping of electrons by beam-aligned modes [34]. The growth of magnetic fields could be observed after this saturation. Their energy density was, however, too low to identify the instability responsible for their growth. A likely candidate is an instability driven by the thermally anisotropic electron distribution [31]. This thermal anisotropy-driven Weibel instability (TAWI) is probably ineffective here because the electrons are rapidly scattered into an isotropic distribution before the magnetic field can grow to a large amplitude. The peak ratio between the electron cyclotron frequency and the plasma frequency remained below 10^{-3}, which is comparable to the equivalent in the ISM.

The electrostatic instability between the beam ions and the heated electrons developed at a later time. It saturated by the trapping of electrons by beam-aligned modes and by obliquely propagating slower modes. The phase space diagram thus revealed the simultaneous development of phase space holes and of the crescent distribution, which was reported first in Ref. [18]. The second mechanism becomes dominant, if the beam speed exceeds by far the electron thermal spread. Here the lower beam speed was such that damping by the the oblique modes was less efficient than the trapping of electrons by beam-aligned modes. Here no magnetic field growth could be observed, probably because of the low phase space density of the thermally anisotropic electron component. We conclude that the TAWI driven by the BTI can not magnetize SNR shocks due to its short life time and low peak amplitude of the magnetic fields.

Acknowledgements: This work was supported by Vetenskapsrådet (DNR 2010-4063), by EPSRC (EP/D043808/1), by Consejeria de Educacion y Ciencia (ENE2009-09276), by the Leverhulme Trust (ECF-2011-383) and by the Junta de Comunidades de Castilla-La Mancha (PAI08-0182-3162). Computer time and support was provided by the HPC2N in Umeå.

[1] J P Eastwood, E A Lucek, C Mazelle, K Meziane, Y Narita, J Pickett, R A Treumann 2005 *Space Sci. Rev.* **118** 41

[2] P J Cargill and K Papadopoulos 1988 *Astrophys. J.* 329 L29

[3] K G McClements, R O Dendy, R Bingham, J G Kirk and L O Drury 1997 *Mon. Not. R. Astron. Soc.* **291** 241

[4] H Schmitz, S C Chapman and R O Dendy 2002 *Astrophys. J.* **570** 637
[5] S C Chapman, R E Lee and R O Dendy 2005 *Space Sci. Rev.* **121** 5
[6] T Umeda, Y Masahiro and R Yamazaki 2008 *Astrophys. J.* **681** L85
[7] S Matsukiyo and M Scholer 2006 *J. Geophys. Res.* **111** A06104
[8] B Lembege, P Savoini, P Hellinger and P M Travnicek 2009 *J. Geophys. Res.* **114** A03217
[9] A M Bykov and R A Treumann 2011 *Astron. Astrophys. Rev.* **19** 42
[10] O Buneman 1958 *Phys. Rev. Lett.* **1** 8
[11] O Buneman 1959 *Phys. Rev.* **115** 503
[12] J M Dawson 1983 *Rev. Mod. Phys.* **55** 403
[13] M E Dieckmann, P Ljung, A Ynnerman and K G McClements 2000 *Phys. Plasmas* **7** 5171 2000
[14] N Shimada and M Hoshino 2003 *Phys. Plasmas* **10** 1113
[15] J Pavan, P H Yoon and T Umeda 2011 *Phys. Plasmas* **18** 042307
[16] M E Dieckmann, K G McClements, S C Chapman, R O Dendy and L O C Drury 2000 *Astron. Astrophys.* **356** 377
[17] N Shimada and M Hoshino 2004 *Phys. Plasmas* **11** 1840
[18] T Amano and M Hoshino 2009 *Phys. Plasmas* **16** 102901
[19] Y Ohira and F Takahara 2007 *Astrophys. J.* **661** L171
[20] M E Dieckmann and A Bret 2008 *New J. Phys.* **10** 013029
[21] E S Weibel *Phys. Rev. Lett.* 1959 **52** 83
[22] A Bret 2007 *Contrib. Plasma Phys.* **47** 113
[23] H H Kaang, C M Ryu and P H Yoon 2009 *Phys. Plasmas* **16** 082103
[24] A Stockem, M E Dieckmann and R Schlickeiser 2009 *Plasma Phys. Controll. Fusion* **51** 075014
[25] L Palodhi, F Califano and F Pegoraro 2009 *Plasma Phys. Controll. Fusion* **51** 125006
[26] A Stockem, M E Dieckmann and R Schlickeiser 2010 *Plasma Phys. Controll. Fusion* **52**, 085009
[27] M E Innocenti, M Lazar, S Markidis, G Lapenta and S Poedts 2011 *Phys. Plasmas* **18** 052104
[28] R C Tautz 2011 *Phys. Plasmas* **18** 012101
[29] D V Romanov, V Y Bychenkov, W Rozmus, C E Capjack and R Fedosejevs 2004 *Phys. Rev. Lett.* **93** 215004
[30] J Niemiec, M Pohl, T Stroman and K Nishikawa 2008 *Astrophys. J.* **684** 1174
[31] R Schlickeiser 2005 *Plasma Phys. Controll. Fusion* **47** A205
[32] EG Berezhko, LT Ksenofontov and HJ Volk 2003 *Astron. Astrophys.* **412** L11
[33] A R Bell 2004 *Mon. Not. R. Astron. Soc.* **353** 550
17 120501
[34] K V Roberts and H L Berk 1967 *Phys. Rev. Lett.* **19** 297
[35] D L Newman, M V Goldman, M Spector and F Perez 2001 *Phys. Rev. Lett.* **86** 1239
[36] C Lancelotti and J J Dorning 2003 *Phys. Rev. E* **68** 026406
[37] A Luque and H Schamel 2005 *Phys. Rep.* **415** 261
[38] G Sarri *et al* 2010 *Phys. Plasmas* **17** 010701
[39] MY Wu, QM Lu, C Huang and S Wang 2010 *J. Geophys. Res.* **115** A10245
[40] D Prono, B Ecker, N Bergstrom and J Benford 1975 *Phys. Rev. Lett.* **35** 438
[41] J W Eastwood 1991 *Comput. Phys. Commun.* **64** 252
[42] W L Kruer, J M Dawson and R N Sudan 1969 *Phys. Rev. Lett.* **23** 838
[43] ME Dieckmann, A Ynnerman, SC Chapman, G Rowlands and N Andersson 2004 *Phys. Scripta* **69** 456
[44] L Romagnani *et al* 2008 *Phys. Rev. Lett.* **101** 025004
[45] G Sarri, GC Murphy, ME Dieckmann, A Bret, K Quinn, I Kourakis, M Borghesi, LOC Drury and A Ynnerman 2011 *New J. Phys.* **13** 073023